Lu *et al. Microstructures* 2022;2:2022017
DOI: 10.20517/microstructures.2022.14

Microstructures

Research Article

Open Access

Detwinning/twin growth-induced phase transformation in a metastable compositionally complex alloy

Wenjun Lu[1], **Fengchao An**[1], **Christian H. Liebscher**[2]

[1]Department of Mechanical and Energy Engineering, Southern University of Science and Technology, Shenzhen 518055, Guangdong, China.
[2]Max-Planck-Institut für Eisenforschung, Max-Planck-Straße 1, Düsseldorf 40237, Germany.

Correspondence to: Prof. Wenjun Lu, Department of Mechanical and Energy Engineering, Southern University of Science and Technology, 1088 Xueyuan Blvd, Nanshan, Shenzhen 518055, Guangdong, China. E-mail: luwj@sustech.edu.cn; Prof. Christian H. Liebscher, Max-Planck-Institut für Eisenforschung, Max-Planck-Straße 1, Düsseldorf 40237, Germany. E-mail: liebscher@mpie.de

How to cite this article: Lu W, An F, Liebscher CH. Detwinning/twin growth-induced phase transformation in a metastable compositionally complex alloy. *Microstructures* 2022;2:2022017. https://dx.doi.org/10.20517/microstructures.2022.14

Received: 9 Jun 2022 **First Decision:** 29 Jun 2022 **Revised:** 11 Jul 2022 **Accepted:** 8 Aug 2022 **Published:** 12 Aug 2022

Academic Editors: Zibin Chen, Jian Wang **Copy Editor:** Fangling Lan **Production Editor:** Fangling Lan

Abstract

Extensive experiments have shown that the transformation from the face-centered cubic to hexagonal close-packed ε phase usually occurs around coherent Σ3 boundaries. However, in this letter, we reveal a different transformation mechanism in a metastable dual-phase compositionally complex alloy via a systematic high-resolution scanning transmission electron microscopy analysis. The face-centered cubic γ matrix can be transformed to the hexagonal close-packed ε phase (as small as one unit) around an incoherent Σ3 boundary (~30 nm), i.e., the facet of the coherent Σ3 boundary. This transformation is assisted by the detwinning/twin growth of a coherent Σ3 boundary during annealing treatment (900 °C for 60 min).

Keywords: Detwinning/twin growth, incoherent Σ3 boundary, 9R structure, displacive transformation, compositionally complex alloy

INTRODUCTION

Phase transformation-assisted alloys have motivated investigations due to their exceptional mechanical properties and excellent application potential in advanced technologies[1-6]. However, a key bottleneck that

hinders their widespread applications is the traditional strength-ductility trade-off[7]. It was recently reported that dual-phase compositionally complex alloys (CCAs) could overcome this hurdle[8-12]. The dual-phase non-equiatomic FeMnCoCr CCA contains face-centered cubic (FCC) γ and hexagonal close-packed (HCP) ε phases, which are obtained by successive cold rolling, annealing above 900 °C and water quenching[8]. Owing to the metastable FCC γ and stable HCP ε phases at room temperature, the mechanical deformation can actively promote the transformation from FCC γ to HCP ε phase[4,5,11]. Such a phase transformation mainly contributes to the work hardening and thus optimizes the strength and ductility simultaneously.

Generally, the displacive transformation from the FCC γ to HCP ε phase is preferentially initiated at high-angle grain boundaries (HAGBs) or the grain interior with a high dislocation density[8,9]. A Σ3 twin boundary is not an ideal nucleation site for the γ→ε phase transformation, owing to its perfect coincidence site lattice (…ABCABACBA… stacking) and low energy state[13]. For a coherent Σ3 boundary, the grain orientation[14], chemical segregation[1,15,16], internal stresses[1,17] and temperature effect[18] can play key roles in promoting the phase transformation. However, the effects of incoherent Σ3 boundary segments (i.e., de-twinning/twin growth processes)[19,20] on the phase transformation are still ambiguous.

In the present work, the microstructure of a dual-phase $Fe_{50}Mn_{30}Co_{10}Cr_{10}$ (at.%) CCA subjected to a high-temperature annealing treatment and subsequent water quenching is examined, focusing on the displacive transformations at the twin boundaries. We observe that the HCP ε phase is formed at the 9R structure, which is attached to the phase boundaries of the nanoscale {112} incoherent twin boundary[21-24]. The phase transformation mechanisms are systemically investigated through multiple electron microscopies and discussed based on kinetics and thermodynamics.

MATERIALS AND METHODS

In this letter, an ingot of a quaternary dual-phase CCA (40 mm × 40 mm × 6 mm) with a nominal composition of Fe-30Mn-10Co-10Cr (at.%) was cast by vacuum induction melting using pure metals (> 99.5 wt.% purity). The ingot was then hot rolled at 900 °C with a thickness reduction ratio of 50% and homogenized for 2 h at 1200 °C in high-purity argon gas flow, followed by water quenching. In order to obtain a proper recrystallized grain size and phase fraction for later analysis, cold rolling was conducted on the homogenized CCA with a thickness reduction ratio of 60%, followed by annealing at 900 °C for 60 min in an argon-protected furnace and water quenching. The recrystallized sample surface was mechanically ground with silicon carbide abrasive paper (P60 to P4000) and then polished using 3 and 1 μm diamond suspensions. The final polishing was conducted using a 50 nm SiO_2 suspension to remove the residual stress on the surface. The microstructure of the polished bulk sample (10 mm × 10 mm × 1.2 mm) was characterized by means of scanning electron microscopy (SEM) equipped with an electron backscattered diffraction (EBSD) TSL high-speed detector using a 50 nm step size and a 15-kV acceleration voltage (JEOL-6500 FEG-SEM). Electron channeling contrast (ECC) imaging was conducted using a Zeiss Merlin microscope. For transmission electron microscopy (TEM)/scanning TEM (STEM) observations, a lift-out lamella containing multiple Σ3 twins was cut using a site-specific procedure in a dual-beam focused ion beam/SEM (FEI Helios Nanolab 600i) instrument[25]. The bright/dark-field TEM images and selected area electron diffraction (SAED) patterns were acquired in an image aberration-corrected FEI Titan Themis 80-300 microscope operated at a 300-kV accelerating voltage. High-resolution STEM imaging and energy-dispersive X-ray spectroscopy (EDS) were carried out using a probe aberration-corrected FEI Titan Themis 60-300 with an acceleration voltage of 300-kV. For high-angle annular dark-field (HAADF) imaging, a probe semi-convergence angle of 17 mrad and inner and outer semi-collection angles of the annular detector ranging from 73 to 200 mrad were used[26].

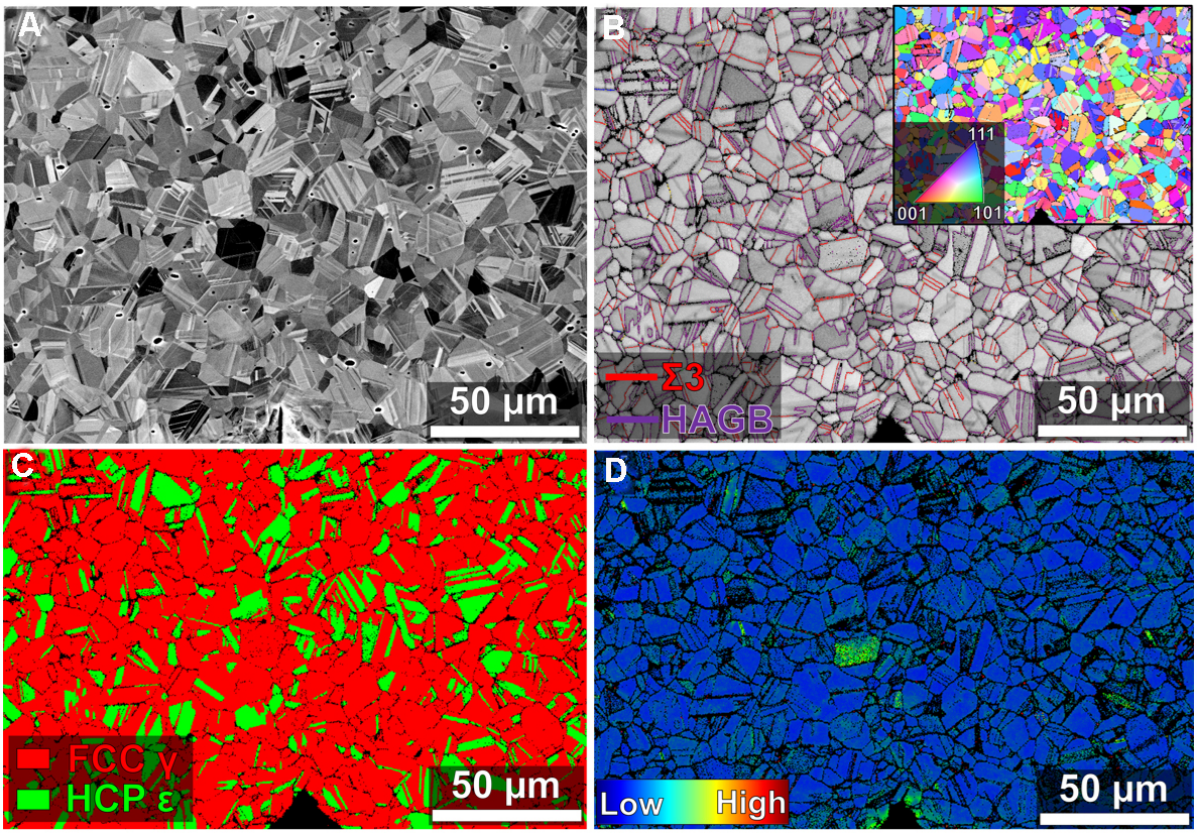

Figure 1. Microstructural characterization for metastable CCA after hot rolling and homogenization. (A) ECC image of the water-quenched sample. (B) EBSD boundary map of same sample region imaged in (A). The inset on the right is the EBSD orientation map. (C and D) Corresponding EBSD phase and KAM maps. The FCC γ and HCP ε phases, Σ3 twin boundary and HAGB are highlighted by red, green, red, and purple, respectively. CCA: Compositionally complex alloy; ECC: electron channeling contrast; EBSD: electron backscattered diffraction; KAM: kernel average misorientation; FCC: face-centered cubic; HCP: hexagonal close-packed; HAGB: high-angle grain boundary.

RESULTS AND DISCUSSION

Figure 1A shows an ECC image of the non-equiatomic CCA. After the annealing treatment, a fully recrystallized CCA with an equiaxed-grained microstructure was obtained. The correlative EBSD data [Figure 1B], including boundary and orientation maps, illustrate that the recrystallized CCA has an average grain size larger than 10 μm with a large amount of annealing twin boundaries (over 42.8 area.%). Further EBSD phase and kernel average misorientation (KAM) maps [Figure 1C and D] show that the CCA has a dual-phase structure containing the FCC γ (69 area.%) and HCP ε (31 area.%) phases with an extremely low dislocation density due to complete recrystallization at high temperature (e.g., 900 °C for 60 min). Upon such a high-temperature recrystallization process, the annealing twins randomly distribute in the FCC γ matrix, while the HCP ε phase is heterogeneously nucleated within the FCC matrix due to the thermal stress induced by the water quenching[8,9,21]. This nucleation behavior of the HCP ε phase may have an intimate connection with the annealing twin boundaries during phase transformation. Further tensile deformation confirms that the annealing twin boundaries are inversely proportional to the HCP ε phase (i.e., Σ3↑; ε↓), as shown in Supplementary Material Figure 1.

Figure 2A shows a representative bright-field TEM image of the CCA containing an annealing twin. The red dashed lines indicate the position of the coherent Σ3 boundaries parallel to the {111} habit plane.

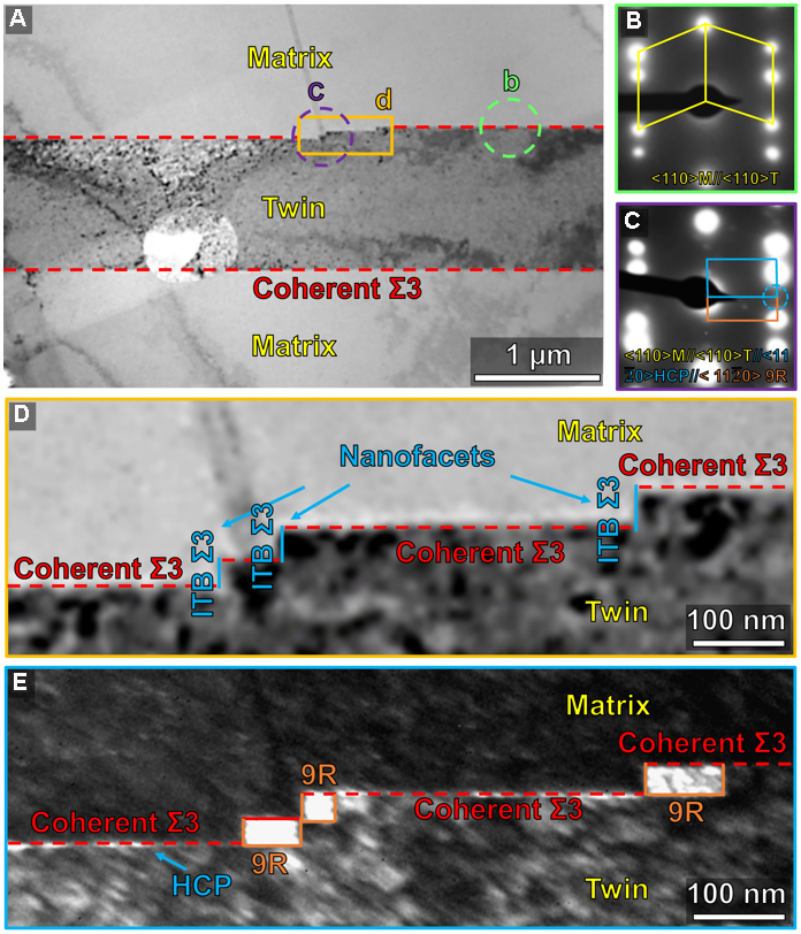

Figure 2. TEM analysis of $Fe_{50}Mn_{30}Co_{10}Cr_{10}$ (at.%) CCA after water quenching. (A) Low-magnification bright-field TEM image of a Σ3 twin within the CCA matrix. The Σ3 twin consists of two coherent Σ3 boundaries (indicated by red dashed lines) and three nanofacets (marked by orange solid square). (B and C) Corresponding SAEDs along the <110>γ zone axis taken from the green and purple dashed circles in (A), respectively. (D) High-magnification bright-field TEM image of Σ3 twin boundary from (A). Three nanofacets are referred to as incoherent Σ3 boundary boundaries (ITBs) and highlighted in blue. (E) Corresponding dark-field TEM image of (D) obtained using the reflection marked by the blue dashed circle in (C). TEM: Transmission electron microscopy; CCA: compositionally complex alloy; SAEDs: selected area electron diffractions.

Figure 2B and C show the corresponding SAEDs of the regions marked by green and purple dashed circles, respectively, in Figure 2A. Different from the coherent Σ3 boundary in Figure 2B, Figure 2C shows a special Σ3 boundary with mixed diffractions composed of the twin, 9R structure and HCP ε phase. The orientation relationships among the matrix, twin, 9R structure and HCP ε phase are determined to be $\{111\}_{matrix}//\{111\}_{twin}//\{0001\}_{9R}//\{0001\}_{HCP}$;$<110>_{matrix}//<011>_{twin}//<11\text{-}20>_{9R}//<11\text{-}20>_{HCP}$[22,23]. Figure 2D presents an enlarged area of this abnormal Σ3 boundary cropped by an orange solid square in Figure 2A. From this image, there are three obvious steps, i.e., nanofacets (~30 nm), visible within the coherent Σ3 boundaries. These nanofacets are parallel to the {112} habit plane, which corresponds to the incoherent Σ3 boundary[21]. Using one of the diffraction spots marked by a blue dashed circle in Figure 2C, a corresponding dark-field TEM image of the 9R structure is obtained from the same position in Figure 2D, as shown in Figure 2E. From this image, it is observed that the 9R structures (~30-80 nm) extend from the incoherent Σ3 boundaries, indicating that they are formed by partial dislocation movement[21]. Furthermore, a weak contrast from the HCP ε phase is found around the coherent Σ3 boundary near the 9R structure. This can be confirmed by further high-resolution STEM analysis in the next section.

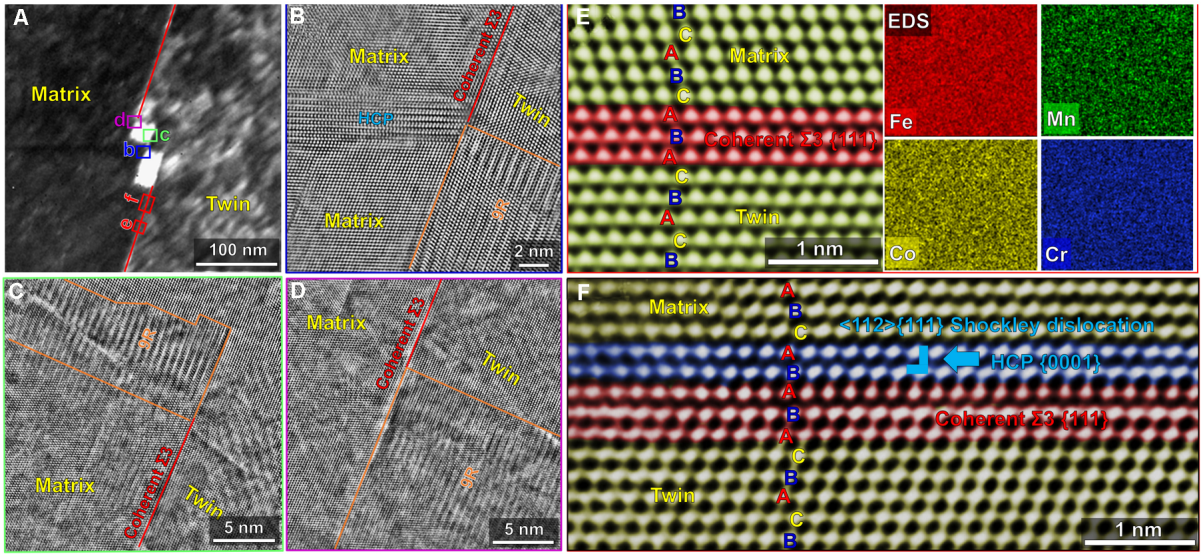

Figure 3. (A) Dark-field TEM image of region shown in Figure 2D. (B-D) High-resolution HAADF-STEM images of Σ3 twin boundary from three different positions, b-d marked in (A). (E) High-resolution HAADF-STEM image from (A) showing a triple atomic layer of a coherent Σ3 boundary with ABA stacking sequence. The corresponding EDS maps indicate a homogenous distribution of the four principle elements, i.e., Fe, Mn, Co and Cr. (F) High-resolution HAADF-STEM image from (A) showing a double atomic layer of HCP ε phase with BA stacking sequence formed by gliding of a leading Shockley partial dislocation. The matrix, coherent Σ3 boundary, 9R structure and HCP ε phase are highlighted by yellow, red, orange, and blue, respectively, in all HAADF-STEM images. TEM: Transmission electron microscopy; HCP: hexagonal close-packed; HAADF: high-angle annular dark-field; STEM: scanning transmission electron microscopy; EDS: X-ray spectroscopy.

Figure 3 shows the TEM/STEM analysis of the nanofacets in Figure 2. For the sample regions marked by blue, green and purple solid squares in the dark-field TEM image [Figure 3A], high-resolution HAADF-STEM is utilized to characterize the atomic configuration at the corresponding positions [Figure 3A-D] near the nanofacets. In these regions, the 9R structures are bounded by two phase boundaries and their atomic stacking parallels to the {0001} habit plane. In addition, the direct proximity of the 9R structures to incoherent Σ3{112} boundaries indicates that they have nucleated from there and then grow along the direction parallel to the {111} coherent Σ3 boundary. This suggests that the formation of the 9R structures stems from the emission of partial dislocations from the incoherent Σ3 boundary under the thermal stresses imposed by water quenching[21,22,27]. Figure 3E and F show high-resolution HAADF-STEM images of the coherent twin boundary for the positions ~50 and ~20 nm away from the 9R structure, respectively. As shown in Figure 3E, a perfect twin structure with …ABCABACBA… stacking[28] is observed ~50 nm away from the 9R structure. Further STEM-EDS analysis [Figure 3E] shows that four principle elements (Fe, Mn, Co and Cr) are homogeneously distributed. However, the Σ3 boundary in close proximity to the 9R structure (…ABCBCACAB…) [Figure 3B-D] only ~20 nm away adopts a different atomic arrangement with …ABCABABACBA… stacking [Figure 3F]. The additional BA stacking around the coherent Σ3 boundary corresponds to one stacking fault or one unit of the HCP ε phase[1]. The presence of this additional HCP ε phase indicates that the phase transformation from the FCC γ to HCP ε phase at the coherent Σ3 boundary initiates from the 9R structure and its phase boundary, which is composed of an array of partial dislocations[21,22,27].

We now discuss the details of the phase transformations at the annealing twin boundaries after the high-temperature treatment. Figure 4 shows an overview of the displacive transformations at different stages. Initially, nanoscale incoherent twin boundaries [Figure 4A] with {112} habit planes are either generated by twin growth or detwinning by the gliding of partial dislocations (i.e., processes with a set of partial

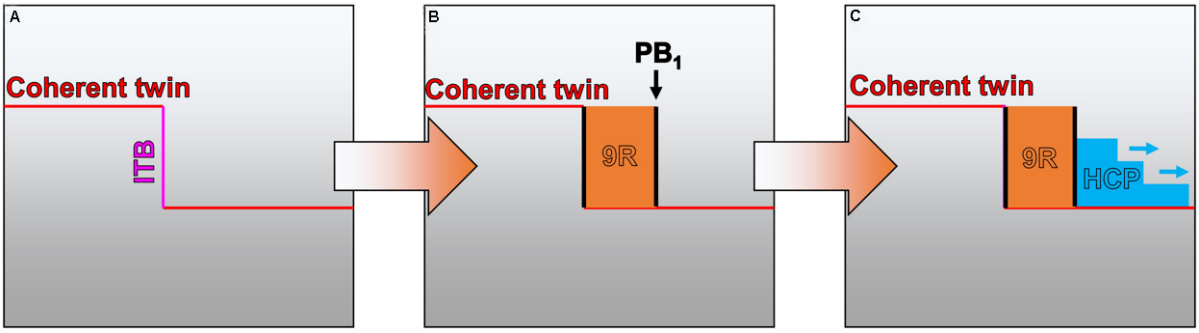

Figure 4. Schematic mechanism of detwinning/twin growth-induced phase transformations at a Σ3 boundary after water quenching. (A) Formation of incoherent twin boundary along the coherent twin boundary. (B) Generation of 9R structure from incoherent twin boundary. (C) Promotion of HCP phase near 9R structure. HCP: Hexagonal close-packed.

dislocations: b_1-edge dislocation; b_2-screw dislocation; b_3-screw dislocation)[21]. Since the mobility of the edge dislocation, b_1 is higher than that of the screw dislocations, b_2 and b_3[22], the 9R structure can be spontaneously formed from the incoherent Σ3 boundary by the motion of b_1 during water quenching (i.e., thermal stresses), as shown in Figure 4B. Such a 9R structure is bounded by two-phase boundaries, which effectively are an array of regularly spaced partial dislocations[21,22]. Such dislocations can actively promote the formation of stacking faults (i.e., Shockley partial dislocations) around the phase boundary of the 9R structure and eventually produce the HCP ε phase via the overlapping of stacking faults [Figure 4C]. From a thermodynamic perspective, the 9R structure usually has a higher Gibbs free energy than that of the matrix (e.g., 357-484 mJm^{-2} in Al and 590-714 mJm^{-2} in Cu)[29]. Such a significant energy difference can be a driving force to promote the formation of the HCP ε phase. Furthermore, based on ab initio calculations of a CrCoNi medium entropy alloy, it is argued that the metastable 9R phase (with a formation energy of -4.809 eV) can induce the stable HCP ε phase (with a formation energy of -4.815 eV) inside the FCC matrix (with a formation energy of -4.808 eV)[30]. Different from the incoherent Σ3 boundary with the 9R structure, the coherent Σ3 boundary is not an ideal nucleation site for the phase transformation from the FCC γ to the HCP ε phase, owing to its perfect coincidence site lattice and low energy state[13,31,32]. This suggests that the HCP ε phase observed along the coherent Σ3 boundary is generally originating from the 9R structure rather than the coherent Σ3 boundary itself. This also clarifies why the HCP ε phase mainly forms along one side of the coherent Σ3 boundary rather than both sides [Figure 4C]. This phase transformation mechanism is thus fundamentally different from those induced by grain orientation, chemical segregation, internal stress and temperature[1,14,15,17].

CONCLUSIONS

In this study, we revealed and discussed the phase transformation around annealing twins in a metastable compositionally complex alloy after water quenching via a systematic high-resolution scanning transmission electron microscopy analysis. The main conclusions are summarized as follows:

1. The FCC γ matrix can be transformed to the HCP ε phase (as small as one unit) around an incoherent Σ3 boundary (~30 nm), i.e., the facet of the coherent Σ3 boundary.

2. The incoherent Σ3 boundary and associated 9R structures (~30-80 nm) can serve as nucleation sites for such a γ→ε phase transformation.

3. The phase transformation is assisted by the detwinning/twin growth of a coherent Σ3 boundary during annealing treatment (900 °C for 60 min).

4. This finding provides novel insights into the nature of phase transformations at twin boundaries in a non-equiatomic dual-phase compositionally complex alloy.

DECLARATIONS

Authors' contributions

Design: Lu W
Experiments: Lu W
Data analysis: Lu W
Manuscript writing: Lu W, An F, Liebscher CH
Manuscript revision and supervising: Lu W, Liebscher CH

Availability of data and materials

Not applicable.

Financial support and sponsorship

Wenjun Lu is grateful for financial support from the open research fund of Songshan Lake Materials Laboratory (2021SLABFK05) and the Shenzhen Science and Technology Program (JCYJ20210324104404012). The authors acknowledge the use of the facilities at the Southern University of Science and Technology Core Research Facility.

Conflicts of interest

All authors declared that there are no conflicts of interest.

Ethical approval and consent to participate

Not applicable.

Consent for publication

Not applicable.

REFERENCES

1. Koizumi Y, Suzuki S, Yamanaka K, et al. Strain-induced martensitic transformation near twin boundaries in a biomedical Co-Cr-Mo alloy with negative stacking fault energy. *Acta Materialia* 2013;61:1648-61.
2. Harjo S, Tsuchida N, Abe J, Gong W. Martensite phase stress and the strengthening mechanism in TRIP steel by neutron diffraction. *Sci Rep* 2017;7:15149. DOI PubMed PMC
3. Sohn SS, Song H, Jo MC, Song T, Kim HS, Lee S. Novel 1.5 GPa-strength with 50%-ductility by transformation-induced plasticity of non-recrystallized austenite in duplex steels. *Sci Rep* 2017;7:1255. DOI PubMed PMC
4. Ding L, Hilhorst A, Idrissi H, Jacques P. Potential TRIP/TWIP coupled effects in equiatomic CrCoNi medium-entropy alloy. *Acta Materialia* 2022;234:118049. DOI
5. Chandan AK, Kishore K, Hung PT, et al. Effect of nickel addition on enhancing nano-structuring and suppressing TRIP effect in $Fe_{40}Mn_{40}Co_{10}Cr_{10}$ high entropy alloy during high-pressure torsion. *Int J Plast* 2022;150:103193. DOI
6. Zhang Z, Jiang Z, Xie Y, Chan SLI, Liang J, Wang J. Multiple deformation mechanisms induced by pre-twinning in CoCrFeNi high entropy alloy. *Scripta Materialia* 2022;207:114266. DOI
7. Fu Y, Liu J, Shi J, Cao W, Dong H. Effects of cold rolling reduction on retained austenite fraction and mechanical properties of high-Si TRIP steel. *J Iron Steel Res Int* 2013;20:50-6. DOI
8. Li Z, Pradeep KG, Deng Y, Raabe D, Tasan CC. Metastable high-entropy dual-phase alloys overcome the strength-ductility trade-off.

Nature 2016;534:227-30. DOI PubMed
9. Li Z, Tasan CC, Pradeep KG, Raabe D. A TRIP-assisted dual-phase high-entropy alloy: grain size and phase fraction effects on deformation behavior. *Acta Materialia* 2017;131:323-35. DOI
10. Li Z, Körmann F, Grabowski B, Neugebauer J, Raabe D. Ab initio assisted design of quinary dual-phase high-entropy alloys with transformation-induced plasticity. *Acta Materialia* 2017;136:262-70. DOI
11. Lu W, Liebscher CH, Dehm G, Raabe D, Li Z. Bidirectional transformation enables hierarchical nanolaminate dual-phase high-entropy alloys. *Adv Mater* 2018;30:e1804727. DOI PubMed
12. Gao X, Liu T, Zhang X, Fang H, Qin G, Chen R. Precipitation phase and twins strengthening behaviors of as-cast non-equiatomic CoCrFeNiMo high entropy alloys. *J Alloys Comp* 2022;918:165584. DOI
13. Lu K, Lu L, Suresh S. Strengthening materials by engineering coherent internal boundaries at the nanoscale. *Science* 2009;324:349-52. DOI PubMed
14. Ma L, Wang L, Nie Z, et al. Reversible deformation-induced martensitic transformation in Al0.6CoCrFeNi high-entropy alloy investigated by in situ synchrotron-based high-energy X-ray diffraction. *Acta Materialia* 2017;128:12-21. DOI
15. Moon J, Qi Y, Tabachnikova E, et al. Deformation-induced phase transformation of Co20Cr26Fe20Mn20Ni14 high-entropy alloy during high-pressure torsion at 77 K. *Mater Lett* 2017;202:86-8. DOI
16. Hou J, Li J, Lu W. Twin boundary-assisted precipitation of sigma phase in a high-entropy alloy. *Mater Lett* 2021;300:130198. DOI
17. Heinz A, Neumann P. Crack initiation during high cycle fatigue of an austenitic steel. *Acta Metallurgica Materialia* 1990;38:1933-40. DOI
18. García ADJ, Medrano AM, Rodríguez AS. Formation of hcp martensite during the isothermal aging of an fcc Co-27Cr-5Mo-0.05C orthopedic implant alloy. *Metall Mat Trans A* 1999;30:1177-84. DOI
19. Hung CY, Shimokawa T, Bai Y, Tsuji N, Murayama M. Investigating the dislocation reactions on Σ3{111} twin boundary during deformation twin nucleation process in an ultrafine-grained high-manganese steel. *Sci Rep* 2021;11:19298. DOI PubMed PMC
20. Zhu Q, Kong L, Lu H, et al. Revealing extreme twin-boundary shear deformability in metallic nanocrystals. *Sci Adv* 2021;7:eabe4758. DOI PubMed PMC
21. Wang J, Anderoglu O, Hirth JP, Misra A, Zhang X. Dislocation structures of Σ3 {112} twin boundaries in face centered cubic metals. *Appl Phys Lett* 2009;95:021908. DOI
22. Liu L, Wang J, Gong SK, Mao SX. High resolution transmission electron microscope observation of zero-strain deformation twinning mechanisms in Ag. *Phys Rev Lett* 2011;106:175504. DOI PubMed
23. Li Q, Xue S, Wang J, et al. High-strength nanotwinned Al alloys with 9R phase. *Adv Mater* 2018;30:1704629. DOI PubMed
24. Zhang Y, Li G, Yuan F, et al. Atomic scale observation of FCC twin, FCC→9R and 9R→12R' transformations in cold-rolled Hafnium. *Scripta Materialia* 2022;207:114284. DOI
25. Liebscher C, Radmilović V, Dahmen U, et al. A hierarchical microstructure due to chemical ordering in the bcc lattice: early stages of formation in a ferritic Fe-Al-Cr-Ni-Ti alloy. *Acta Materialia* 2015;92:220-32. DOI
26. Lu W, Herbig M, Liebscher C, et al. Formation of eta carbide in ferrous martensite by room temperature aging. *Acta Materialia* 2018;158:297-312. DOI
27. Wang J, Li N, Anderoglu O, et al. Detwinning mechanisms for growth twins in face-centered cubic metals. *Acta Materialia* 2010;58:2262-70. DOI
28. Zhu Q, Huang Q, Tian Y, et al. Hierarchical twinning governed by defective twin boundary in metallic materials. *Sci Adv* 2022;8:eabn8299. DOI PubMed PMC
29. Tschopp MA, Coleman SP, Mcdowell DL. Symmetric and asymmetric tilt grain boundary structure and energy in Cu and Al (and transferability to other fcc metals). *Integr Mater Manuf Innov* 2015;4:176-89. DOI
30. Zhang Z, Sheng H, Wang Z, et al. Dislocation mechanisms and 3D twin architectures generate exceptional strength-ductility-toughness combination in CrCoNi medium-entropy alloy. *Nat Commun* 2017;8:14390. DOI PubMed PMC
31. Lu L, Shen Y, Chen X, Qian L, Lu K. Ultrahigh strength and high electrical conductivity in copper. *Science* 2004;304:422-6. DOI PubMed
32. Lu L, Chen X, Huang X, Lu K. Revealing the maximum strength in nanotwinned copper. *Science* 2009;323:607-10. DOI PubMed